HHS Public Access

Author manuscript

Ann Biomed Eng. Author manuscript; available in PMC 2016 June 01.

Published in final edited form as:

Ann Biomed Eng. 2015 June ; 43(6): 1385–1397. doi:10.1007/s10439-014-1092-7.

Characterization of abnormal wall shear stress using 4D flow MRI in human bicuspid aortopathy

Pim van Ooij[1], **Wouter V. Potters**[2], **Jeremy Collins**[1], **Maria Carr**[1], **James Carr**[1], **S. Chris Malaisrie**[3], **Paul W.M. Fedak**[4], **Patrick M. McCarthy**[5], **Michael Markl**[1,6], and **Alex J. Barker**[1]

[1]Department of Radiology, Northwestern University, Chicago, IL, USA [2]Department of Radiology, Academic Medical Center, Amsterdam, the Netherlands [3]Department of Medicine-Cardiology, Northwestern University, Chicago, IL, USA [4]Department of Cardiac Surgery, University of Calgary, Calgary, Canada [5]Division of Surgery-Cardiac Surgery, Northwestern University, Chicago, IL, USA [6]Department of Biomedical Engineering, Northwestern University, Chicago, IL, USA

Abstract

There exists considerable controversy surrounding the timing and extent of aortic resection for patients with BAV disease. Since abnormal wall shear stress (WSS) is potentially associated with tissue remodeling in BAV-related aortopathy, we propose a methodology that creates patient-specific 'heat maps' of abnormal WSS, based on 4D flow MRI. The heat maps were created by detecting outlier measurements from a volumetric 3D map of ensemble-averaged WSS in healthy controls. 4D flow MRI was performed in 13 BAV patients, referred for aortic resection and 10 age-matched controls. Systolic WSS was calculated from this data, and an ensemble-average and standard deviation (SD) WSS map of the controls was created. Regions of the individual WSS maps of the BAV patients that showed a higher WSS than the mean+1.96SD of the ensemble-average control WSS map were highlighted. Elevated WSS was found on the greater ascending aorta (35% ± 15 of the surface area), which correlated significantly with peak systolic velocity (R^2=0.5, P=0.01) and showed good agreement with the resected aortic regions. This novel approach to characterize regional aortic WSS may allow clinicians to gain unique insights regarding the heterogeneous expression of aortopathy and may be leveraged to guide patient-specific resection strategies for aorta repair.

Keywords

bicuspid aortic valve; aortopathy; wall shear stress; oscillatory shear index; patient-specific heat map

Corresponding author Pim van Ooij, PhD, Department of Radiology, Northwestern University, 737 N. Michigan Ave., Suite 1600, Chicago, IL 60611, (312)-695-1539, pim.vanooij@northwestern.edu.

INTRODUCTION

With an incidence of 1–2%, bicuspid aortic valve (BAV) disease is responsible for more morbidity and mortality than the combined effects of all other congenital heart defects (0.8% of live births) (1). BAV is related to frequent and premature occurrence of cardiovascular events, dominated by the development of heart failure resulting from aortic valve stenosis, and the development of aortic dilatation (2). Serious complications occur in at least one third of BAV patients, with the incidence of aortic dissection occurring more frequent than in the general population (3,4). Thus, the ability to understand which patients are at risk for developing complications has the potential to greatly improve the standard of care.

Nonetheless, controversy exists regarding the surgical management for BAV aortopathy, especially when considering timing and extent of surgical intervention in an individual patient. For example, the minimum threshold for intervention is subject to clinician preference, with some surgeons intervening at dilated aortic diameters as small as 4.5 cm, while others are known to wait until 5.5 cm (5,6). A recent survey reinforced these gaps in attitude, especially as they relate to the clinical guidelines (7,8). The controversy is also highlighted by the recent changes to the ACC/AHA recommendations for management of patients with BAV-related aortopathy. For example, the threshold aortic diameter for surgery has changed from 5.0 cm (9) to 5.5 cm (8), primarily because few large scale studies have been performed, and of those, few look beyond aortic diameter and growth rate. With the development of more advanced stratification biomarkers, some groups have proposed that guidelines dependent on aortic dimensions are too simplified, and do not account for the underlying pathophysiological mechanisms such as tissue characteristics, valve morphology or hemodynamic shear stresses (10). Therefore, a process is needed which allows for new biomarkers to be evaluated in relation to physiologic norms and to the risk of regional aortic growth or dissection (11).

With this in mind, it is known that aortopathy in the presence of BAV disease is associated with accelerated degeneration of the aortic media, fragmentation of elastic tissue and changes in smooth muscle cell orientation (12) (13,14). These disruptions have also been associated with the abnormal expression of wall shear stress (WSS) (15,16). Recent MRI pilot studies, based on time-resolved, three-dimensional phase contrast MRI (4D flow MRI), have shown that BAV patients do, in fact, express abnormal WSS (17–20). However, these studies have estimated WSS using manually placed planes highly focused on specific vascular landmarks (21). This approach may miss large aortic regions demonstrating abnormal WSS characteristics. Furthermore, the studies averaged WSS in cohort-averaged ensembles, which do not allow for the identification of individual patient cases with abnormal WSS. An individualized approach for assessment of regional wall shear stress is critical to developing individualized resection strategies for patients with BAV aortopathy.

Recently, two studies demonstrated the feasibility of volumetric WSS estimation based on the direct use of 4D flow MRI data, without the need for computational modeling (22,23). In the current study, pre-operative volumetric WSS was used to identify abnormal WSS in individual BAV patients who underwent ascending aortic repair by comparison with an ensemble-average WSS map (24) of healthy volunteers. The aim was to present a large

amount of information in an easy to interpret ‘heat map’, capable of delineating regions of abnormal WSS in single-patient BAV cases by comparing them to WSS maps obtained from ensemble averages of healthy control subjects. In addition, the ascending aortic regions with abnormal WSS were compared to the region of tissue that was resected. Furthermore, ensemble-average WSS maps can be used as *P*-value maps (24) which visualize and quantify regions of significant, ensemble-averaged WSS differences (for example, to show the average difference of WSS expression in various valve morphology phenotypes).

METHODS

Enrollment

Thirteen BAV patients (mean age: 51±17 years old, range: 20–82 years old, all men) referred for pre-surgical MR prior to aortic root replacement with aortic valve repair (or replacement) were enrolled in this study. Eight of the aortic valves were replaced with a bioprosthetic valve, 3 with a mechanical valve, 1 with a pulmonary valve (Ross procedure) and 1 underwent repair. In all patients, the aortic root was replaced by Dacron grafts, with the ascending aorta also replaced in 11 cases. Six of these also included hemiarch replacement. The healthy control cohort consisted of 10 age-matched (P=0.88, Wilcoxon rank sum test) subjects with a tricuspid aortic valve (TAV) and no history of cardiovascular disease (mean age: 50±14 years old, range: 33–76 years old, 6 men and 4 women).

The study was approved by the local Institutional Review Board (IRB). Nine controls and all BAV patients provided informed consent. The tenth control presented normal findings on a clinical scan and was enrolled using an IRB approved protocol permitting retrospective chart review.

MR Imaging

All patients were examined with standard-of-care thoracic cardiovascular MRI on 1.5 and 3T scanners (MAGNETOM Espree, Avanto, Skyra, Aera, Siemens, Erlangen, Germany). Cardiac function and valve morphology were assessed by ECG gated CINE balanced steady state free precession (bSSFP) cardiac MRI. Contrast enhanced MR angiography (CE-MRA, Multihance or Magnevist) was used for the quantification of the aortic diameters. The scan parameters for the CE-MRAs were: spatial resolution = 0.78–1.17 mm × 0.78–1.17 mm × 1.10–1.80 mm; TE/TR/flip angle = 0.9–1.2 ms/2.7–3.4 ms/25–40°; field of view = 273–328 mm × 350–500 mm × 72–106 mm.

2D phase contrast (PC) MRI was performed above and below the valve to assess aortic insufficiency (AI). The scan parameters for the 2D PC-MRI examinations were: spatial resolution = 1.63–2.35 mm × 1.63–2.80 mm × 6–7 mm; TE/TR/flip angle = 1.9–2.7 ms/ 3.69–5.8 ms/20–30°; field of view = 225–366 mm × 244–380 mm.

Additionally, 4D flow MRI was performed in a sagittal oblique volume using prospective ECG gating and free-breathing with a respiratory navigator placed on the lung-liver interface to assess velocity in the three principal directions over time (25). The 4D flow pulse sequence parameters were: spatial resolution = 2.24–3.8 mm × 1.67–2.69 mm × 2.2–3 mm; temporal resolution = 36–43 ms (18±3, 13–25 cardiac time frames); TE/TR/flip angle =

2.2–2.8 ms/4.5–5.4 ms/7–15°; field of view = 144–430 mm × 130–301 mm × 60–116 mm; velocity sensitivity = 150 cm/s and 150–400 cm/s for the controls and the patients, respectively.

Data analysis

BAV valve morphology was classified on bSSFP images at the level of the valve by an experienced radiologist and if possible, corroborated during surgery. BAV AP indicates BAV valves without raphes that open in anterio-posterior direction. BAV lat indicates BAV valves without raphes that open in lateral direction. BAV RL indicates BAV valves with 1 raphe and fusion of the right coronary and left coronary valve. BAV RN indicates BAV valves with 1 raphe and fusion of the right coronary and non-coronary valve. BAV uni indicates BAV valves characterized by two raphes: fusion of the right and left coronary valves and fusion of the right coronary and the non-coronary valves, resulting in a functionally unicuspid valve (26).

In addition, the pattern of aortopathy was classified according to the typology introduced by Fazel et al. (27) and refined by Kang et al. (28). Aortopathy type 1 is characterized by dilation of the aortic root, type 2 by dilation of the root and ascending aorta (AAo) and type 3 by dilation of the root, AAo and transverse aortic arch (28).

An experienced radiologist measured the aortic diameters at the level of the Sinus of Valsalve (SOV) and the mid-ascending aorta (MAA) in Vitrea (version 6.0.0.1, Vital Images, Minnetonka, MN, USA)(29).

Aortic insufficiency (AI) was calculated by dividing forward volume from the 2D PC-MRI measurement above the valve by the retrograde volume from the 2D PC-MRI measurement below the valve. AI was classified as mild, moderate and severe according to a regurgitant fraction less than 29%, between 30 to 49%, or greater than 50%, respectively (30).

The 4D flow MRI measurements were corrected for eddy currents, Maxwell terms and velocity aliasing using home built Matlab software (Natick, the Mathworks, USA) (31). Voxels with remaining velocity aliasing were manually corrected. The 4D flow MRI magnitude images were multiplied by absolute velocity and averaged over time to yield 3D phase contrast angiography (PC-MRA) images (31). The 3D PC-MRA images were used to semi-automatically segment the aortic lumen (MIMICS, Materialise, Leuven, Belgium). The time frame with the maximum average absolute velocity in the segmentation was defined as peak systole. A maximum intensity projection (MIP) was created of the absolute velocity in the aorta. A region of interest in was manually drawn in this MIP to determine the maximum velocity at peak systole.

The maximum velocity at peak systole was used to classify aortic stenosis as is recommended for continuous wave Doppler ultrasound guidelines (mild stenosis: between 1.5–3 m/s, moderate stenosis: between 3–4 m/s, severe stenosis: greater than 4 m/s) (30).

WSS calculation

WSS was calculated using the method developed by Potters et al. (23). In short, the shear stress tensor:

$$\vec{\tau} = 2\eta\dot{\varepsilon} \cdot \vec{n} \quad [1]$$

was simplified by performing a rotation such that the z-axis aligned with the normal vector of the vessel wall, resulting in $\vec{n} = (0,0,1)$. In equation 1 η is the dynamic viscosity (Newtonian: $3.2 \cdot 10^{-3}$ Pa•s), $\dot{\varepsilon}$ is the rate of deformation tensor and $\vec{n}$ is the normal vector orthogonal to the vessel wall. Since no flow occurs through the wall ($\vec{n} \cdot \vec{v} = 0$ at the wall), the inner product of the rate of deformation tensor and the normal vector is reduced to:

$$2\dot{\varepsilon} \cdot \vec{n} = \left(\frac{\partial v_x'}{\partial z'}, \frac{\partial v_y'}{\partial z'}, 0\right) \quad [2]$$

where the shear rates $\frac{\partial v_x'}{\partial z'}$ and $\frac{\partial v_y'}{\partial z'}$ are the spatial velocity gradients at the wall in the rotated coordinate system. Thus, the rotated WSS vector $\vec{\tau}'$ is defined as:

$$\vec{\tau}'_x = \eta\frac{\partial v_x'}{\partial z'}, \vec{\tau}'_y = \eta\frac{\partial v_y'}{\partial z'}, \vec{\tau}'_z = 0 \quad [3]$$

The shear rates were derived from 1D smoothing splines (32) fitted through three equidistant data points along the inward normal vector onto which the rotated surrounding x- and y-velocity values were interpolated. The length of the inward normal was 1.5 cm (23). Subsequently, the WSS vector was transformed to the original coordinate system by inverse rotation. To reduce the influence of noise on the WSS vectors, average WSS vectors were calculated over five cardiac time frames centered at peak systole. 2D slices were manually placed perpendicular to the ascending aorta in three subjects to visualize peak systolic WSS vectors (Ensight, CEI Inc, Apex, NC, USA). For the same subjects, volumetric WSS vectors were visualized in Matlab (The Mathworks, Natick, MA, USA).

Control population: ensemble-averaged WSS maps

As previously reported (24), an ensemble-averaged 3D WSS map representing physiologically ‘normal’ WSS values experienced in the control population was created using a four-step approach, briefly summarized: 1) the 3D segmentations of the control aortas were co-registered (rigid registration using FLIRT (33)) such that a map was created representing the overlap of the segmentations. 2) The amount of overlap (24) between the individual control aortas and geometries with different thresholds was calculated as a measure of anatomic variability. The geometry with the maximum overlap was chosen for the idealized geometry representing the cohort. 3) Each individual control 3D segmentation was registered (affine registration in FLIRT) to the geometry, and WSS in each control subject was subsequently interpolated to the geometry using nearest neighbor interpolation. The difference in mean velocity before and after interpolation (24) was calculated in six regions to indicate a budget of uncertainty. 4) The interpolated WSS was averaged over all

control subjects, resulting in a ensemble-averaged 3D WSS map and a standard deviation (SD) WSS map.

Heat maps: comparison of single subject regional WSS variation to physiologic norms

In order to detect if the regional expression of 3D WSS in the aorta of a single BAV patient was outside of that expected for healthy, normal physiology (as defined by the ensemble-average of the control group), heat maps were generated which represent locations where patients exhibited abnormal shear characteristics. Thus, the individual BAV geometry was registered to the ensemble-averaged control geometry and the ensemble-averaged 3D WSS map and SD WSS map interpolated to the individual aorta geometry of the BAV patient (figure 1A and B). Next, the ensemble-average and SD maps for WSS were combined (mean ± 1.96*SD maps, figure 1C) and compared with the individual BAV patients to create the heat maps (figure 1D). Regions where WSS for the individual BAV patient was higher than the mean + 1.96 times the SD of the control population are highlighted in red. Regions where WSS for the individual BAV patient was lower than the mean − 1.96 times the SD of the control population are highlighted in blue. Regions that were within range were delineated in grey.

P-value maps: comparison of patient population regional WSS variation to physiologic norms

To compare the BAV patient population with the control population, each WSS profile of the individual BAV patient was registered and interpolated to the control population aortic geometry (figure 2A and B). The WSS map of the BAV patient population was then tested for significance on a voxel-by-voxel basis to the control population, allowing for *P*-value maps to be created (figure 2C).

Statistical Analysis

To create the *P*-value maps for WSS, a Wilcoxon rank sum test between the individual BAV patients and controls was performed for each location on the control aorta geometry (24) (figure 2C). Differences were considered statistically significant for $P<0.05$. Significant regional differences of WSS between cohorts were visualized in red and blue when the WSS of the patients was respectively greater and lower than the controls. Regions where the difference was not significant were delineated in grey.

To quantify the results, the segmented aorta was manually subdivided into six regions for which the difference in mean velocity before and after interpolation and the percentage of the aorta surface that is abnormally higher or lower than the controls is reported. The six regions include: 1) the inner curvature of the ascending aorta (AAo), 2) the outer curvature of the AAo, 3) the inner curvature of the aortic arch, 4) the outer curvature of the arch, 5) the inner curvature of the descending aorta (DAo) and 6) the outer curvature of the DAo (see figure 4).

All values are expressed as a mean ± SD percentage of surface area of the region of interest shown in figure 3. Correlations between peak systolic velocity, aortic dimensions and percentage of the surface where WSS was higher for the BAV patients (as compared to the

controls) were investigated using univariate linear regression. The strength and significance of the correlations were calculated and expressed as R^2 and *P*-value, respectively. $P<0.05$ was considered significant.

RESULTS

In table 1 the aortic dimensions, valve morphology, aortopathy phenotype, AI and AS severity of the BAV patients and controls are summarized.

WSS calculation

In figure 3, peak systolic volumetric WSS vectors and WSS vectors in a slice placed perpendicular to the aorta are shown. The choice of slice placement is based on the hypothesis that flow patterns distal to RL-fusion valves are directed toward the right anterior wall of the root and aorta, exerting high WSS and promoting dilation of the root and mid-ascending aorta. Flow patterns distal to RN-fusion valves are believed to be reflected off the posterior wall of the root, and exert high WSS more distal to the RL-fusion pattern (potentially promoting dilation involving regions near the arch)(34). WSS in the control aorta shows similar WSS vectors around the circumference of the aorta for both images, whereas WSS patterns for the BAV patients are highly asymmetric.

Control population: ensemble-averaged WSS maps

In figure 4a the anatomic variability for the co-registered control aortas is shown in a maximum intensity projection. The maximum amount of overlap (26±7%) was found for a threshold of ≥ 4 overlapping aortas, resulting in the idealized geometry shown in figure 4b. The standard deviation of 7% illustrates the small anatomic variability of the control aorta geometries.

Heat maps: comparison of single subject regional WSS variation to physiologic norms

The maximum amount of overlap between the idealized control geometry and the individual BAV patients was 39±9%, illustrating the slightly higher variability in aortic anatomy for the BAV patients. The amount of overlap for registration of the ensemble-averaged control geometry to the BAV patients was significantly different from the amount of overlap for registration of the individual control geometries to the ensemble-averaged control geometry (Wilcoxon rank sum test, P=0.005). The interpolation of the ensemble-averaged control WSS to the individual BAV geometries resulted in mean velocity differences of 2±1% for the inner ascending aorta, 2±2% for the outer ascending aorta, 5±3% for the inner arch, 5±3% for the outer arch, 3±2% for the inner descending aorta and 1±1% for the outer descending aorta, resulting in a total budget of uncertainty of 3%.

Figure 5 depicts WSS heat maps and the area of resected tissue for all BAV patients included in the study. In most aortas, abnormal WSS was elevated (red) on the greater curvature of the ascending aorta (mean percentage of the surface: 35% ± 15), see figure 5 and table 2. For all six regions, the percentage of abnormally depressed WSS (blue regions) was on the order of 0–1%. In most cases the regions of resected tissue corresponded with the regions of abnormally elevated WSS.

Interactions: traditional disease biomarkers and WSS

For the BAV patient population, a significant correlation (R^2=0.5, *P*=0.01) was found between peak systolic velocity in the aortic outflow region and the percentage of the greater curvature of the ascending aorta with elevated WSS (red area in region 2 of figure 3).

A trend was found towards a negative correlation (R^2=0.3, *P*=0.06) between the SOV diameter and the percentage of the greater curvature of the ascending aorta surface area (region 2 in figure 3) with higher WSS (red areas in figure 3).

No correlations were found for abnormal WSS surface percentages and cardiac output, heart rate or body surface area.

Table 3 shows a trend for increasing surface area with elevated WSS in the BAV patient population on the inner and outer AAo curvature as a function of valve phenotype (i.e. abnormal WSS surface area increases from phenotype AP, lat, RN, RL and unicuspid valve morphology).

P-value maps: comparison of patient population regional WSS variation to physiologic norms

Similar to the single-subject results, significantly higher WSS was found on the outer curvature of the ascending aorta for the ensemble-averaged BAV group, as compared to the control group. Isolated regions of depressed WSS were found at the inner curvature of the ascending aorta and arch (figure 6a, table 3).

DISCUSSION

In this study, a proof of concept was presented that allows for visualization of abnormal aortic WSS in individual BAV patients by comparing regional WSS with the population-average of age-matched healthy controls. For all BAV patients, elevated WSS was found in the ascending aorta compared to healthy controls. On average, abnormally depressed WSS was lower than 1% and therefore considered negligible. The technique allows for a comprehensive, easy-to-grasp evaluation of abnormal relative wall shear stress and has the potential to clarify the relationships between altered hemodynamics due to valve morphology and aortopathy in BAV disease.

Finite element methods (FEM) and computational fluid dynamics (CFD) are frequently used for the evaluation of hemodynamics in BAV disease. FEM models provide valuable insights in increased stress exerted on the bicuspid valve compared to the tricuspid valve (35,36). CFD has the ability to simulate aortic blood flow in BAV disease, and the main outcomes of these studies correspond to the results of this study, i.e. maximum WSS at the outer curvature of the mid-ascending aorta (37–39).

In this study, all measurements were derived directly from the acquired imaging data. The approach is advantageous in that it does not require the assumption of inlet and boundary conditions. CFD has progressed significantly over the last few years in terms of prescribing boundary conditions (now frequently measured with 4D flow MRI (40)) and fluid-structure

interaction (41), however, we chose to use an approach which uses the direct data from the MRI sequence. This approach required less processing, computational power, and need for model assumptions. Future applications may realize a spatio-temporal benefit through the use of a hybrid image-based CFD approach. Nonetheless, in its current implementation, the 4D flow MRI measurement, subsequent data post-processing and the application of the technique presented in this paper can be completed within 2 hours, potentially providing a bridge solution for use in the clinic.

The registration and interpolation steps necessary to create ensemble-averaged WSS maps and heat maps can lead to some uncertainties in WSS profiles. The rigid and affine registration processes can possibly fail when the anatomic variability is high. However, this was not observed in the cohorts used in this study which is supported by the moderate anatomic variability for the ensemble-averaged control WSS map (7%) and for the BAV patients (9%). Therefore, there was no need to guide the registration process by attributing landmarks or normalize the aorta geometries. Furthermore, the budget of uncertainty for interpolation of the ensemble-averaged control WSS map to the individual BAV patients was small (3%). Therefore, the technique applied to the cohorts used in this study is easy-to-use and robust.

P-value maps were used to detect statistically abnormal WSS in the BAV patients, as compared to physiologic ensemble-averaged norms (using a previously described method) (24). These approaches are intended as a first-step towards large-scale tissue and population studies investigating if WSS is a risk factor for regional vascular remodeling. The individualized analysis revealed increased WSS on the greater curvature of the ascending aorta in the majority of the BAV heat maps, which is also supported by the BAV cohort WSS *P*-value map. Note that similar results were found for patients with tricuspid valve stenosis (24). Preliminary studies have shown that the greater curvature in BAV patients is also known to have an altered molecular expression of MMP (14,42–44) and eNOS (45,46). Nonetheless, regional inter-patient variation is apparent and indicative of the important role of individual valvular and vascular anatomy, and its potential impact on inter-patient variation.

The percentage of surface area with increased WSS on the greater curvature of the AAo correlated with peak systolic velocity in the aortic outflow region (R^2=0.5, *P*=0.01). This correlation agrees with the observations of high velocity jets impinging on the greater curvature of the aorta, with recirculating flow occurring at the inner curvature (17,47). Additionally, the relationship between elevated velocity and elevated shear is an important finding, as aortic stenosis (e.g. elevated transvalvular velocities) was found to be one of the most powerful predictors for aortic aneurysm formation in BAV patients (multivariate odds ratio 3.4, n=416 followed over 29 years)(3). Consequently, a compelling connection seems to exist between peak velocity, elevated WSS, a mechanotransduction pathway capable of influencing vascular remodeling, and evidence of longitudinal risk for aneurysm. While care must be taken given that all patients were pre-surgically referred for valve or aneurysm repair, it is notable that abnormal shear was found in the inner and outer curvature of the AAo (table 4). A number of these regions were chosen for resection. This illustrates the

potential of the proposed methodology to aid in surgical planning (if WSS is, indeed, found to be associated with aneurysm growth).

Interestingly, a trend was found for a relation between increasing surface percentages of elevated WSS with BAV morphology type. In a previous study, it was shown that unicuspid valves presented higher flow angles than lat, AP, RN and RL valve morphology (26). Higher flow angles may cause larger areas of elevated WSS than low flow angles, which is congruent with lower areas of elevated WSS for lat, AP, RN and RL than unicuspid valves found in this study. Figures 3 and 4 support the mechanotransduction hypothesis that aortopathy mediated by abnormal WSS is the result of the RL-fusion impacting wall forces at the aortic root and proximal aorta, whereas RN-fusion appears to impact the wall forces more distal in the ascending aorta with involvement of the arch (34).

An effort was made to associate the surface area with higher WSS to SOV and MAA diameter. However, no significant correlations were found (although, trends did exist). The lack of statistical significance may be due to the low number of subjects investigated, the cross-sectional study design, or that simply no relationship exists to aneurysm growth (48). To robustly investigate if abnormal WSS relates to aortic dimensions or growth, additional subjects and longitudinal data are needed. However, the trend for smaller surface areas of elevated WSS for larger aortic diameters is in accordance with previous studies that show that aortas with larger diameters are associated with lower WSS (22,49). No trends or significant differences were found between aortopathy type and the percentage of regional aorta surface with higher WSS or OSI.

The *P*-value map can provide a generalized representation of abnormal WSS for an entire patient group (such as a type 1 RL-only group versus a type 1 RN-only group). Interestingly, the WSS *P*-value map for the BAV patient population resembles the *P*-value map for dilated aortas with TAV stenosis as presented in a previous study (24), presenting similar percentages of aorta surface of increased WSS. This may be an indication of similar behavior of flow and WSS for BAV and TAV with stenosis, potentially leading to wall changes in both patient cohorts (50). With more subjects, separate *P*-value maps can be created for the different bicuspid valve morphologies, specifically focusing on how WSS is impacted in the presence of different fusion patterns. The finding of different locations of elevated WSS for type 1 RL and type 1 RN valve morphology by planar analysis (51) can be verified in more detail by this *P*-value map methodology. Future patient management could use this information to understand to what extent and at which locations the aorta may be at risk for dilation.

Study Limitations

Since the image SNR and blood flow velocity in diastolic cardiac phases is generally low, the PC-MRA images used for aortic segmentation are dominated by the systolic phases. Therefore, the motion of the aorta during the cardiac cycle limits the segmentations used in this study for use over the systolic phases. Using 2D PC-MRI imaging, and a time-resolved approach to segmentation, we have shown that WSS in the diastolic phases ‘dilutes’ the patient/control differences when averaging over the cardiac cycle (18). Therefore, in light of

these results, and the difficulty of a time-resolved 3D segmentation using the approach described here, we chose not to report WSS over the diastolic phases.

The main goal of this study was to present a methodology to visualize patient-specific WSS abnormalities by comparison with an ensemble-average of the control population WSS maps. The relatively low number of BAV patients did not allow for stratification of those with aortic insufficiency or stenosis. It is expected that with the inclusion of more BAV patients the significances detected here will improve in power and a more detailed analysis for insufficiency, valve morphology and aortopathy type can be performed. For the WSS *P*-value maps, however, the number of subjects was sufficient to reach a statistical power assuming a mean ± SD systolic WSS of 0.4 ± 0.2 Pa for both the controls and the BAV patients ($P<0.05$) (17).

The cut-off value for the individualized analysis of ±1.96*SD was chosen to represent WSS values outside of the 95% confidence interval for normal shear values; the surface area of abnormal shear will enlarge or shrink depending on threshold values. Varying cut-off values was outside the scope of this study since the main goal was to present the technique, but future work will include a detailed analysis of sensitivity and specificity for varying thresholds (±0.5*SD, ±1*SD etc).

The 4D flow MRI examinations were performed on both 1.5 and 3T scanners. Due to different SNR levels, the accuracy of the WSS calculations may be slightly higher using 3T data than 1.5T data. Note, however, that Strecker et al. (52) did not find any significant differences in planar WSS between 1.5 and 3T. It is therefore expected that our results are not influenced substantially by field strength differences. In addition, the accuracy of WSS measurements will depend on spatial resolution and segmentation of the vessel (53). However, the segmentation algorithms were identical and the spatial resolution was similar for all subjects, thus, the relative values between subjects can be compared, irrespective of absolute error. For example, the visualization and quantification of higher or lower WSS as compared to controls, rather than reporting absolute WSS numbers, was emphasized in this study to minimize concerns related to the ability to measure absolute WSS. Validation of the WSS calculation method by comparison with CFD was outside the scope of this study. Nonetheless, good agreement between WSS calculated with CFD and 4D flow MRI was shown in carotid arteries (54) and in an in vitro and in vivo intracranial aneurysms (55), albeit with the expected lower absolute WSS values for 4D flow MRI. Future work will include a detailed analysis of scan/rescan, and intra- / inter-observer variability for WSS.

In conclusion, this pilot study presents a methodology to create heat maps for visualization and quantification of abnormal WSS in individual and ensemble-averaged BAV patients. These techniques have the potential to aid studies assessing the importance of WSS when considering risk for aortopathy. In addition, the use of these techniques pre-intervention can be used to investigate resected tissue for markers associated with vascular remodeling. In the future, the approaches presented here may aid in developing BAV phenotype or patient specific resection strategies for patients requiring ascending aorta repair.

Acknowledgments

FUNDING SOURCES: NIH NHLBI grant R01HL115828; American Heart Association Scientist Development Grant 13SDG14360004; Dutch Technology Foundation (STW) Carisma Grant 11629.

REFERENCES

1. Ward C. Clinical significance of the bicuspid aortic valve. Heart. 2000; 83(1):81–85. [PubMed: 10618341]
2. Michelena HI, Desjardins VA, Avierinos JF, Russo A, Nkomo VT, Sundt TM, Pellikka PA, Tajik AJ, Enriquez-Sarano M. Natural history of asymptomatic patients with normally functioning or minimally dysfunctional bicuspid aortic valve in the community. Circulation. 2008; 117(21):2776–2784. [PubMed: 18506017]
3. Michelena HI, Khanna AD, Mahoney D, Margaryan E, Topilsky Y, Suri RM, Eidem B, Edwards WD, Sundt TM 3rd, Enriquez-Sarano M. Incidence of aortic complications in patients with bicuspid aortic valves. JAMA. 2011; 306(10):1104–1112. [PubMed: 21917581]
4. Roberts CS, Roberts WC. Dissection of the aorta associated with congenital malformation of the aortic valve. J Am Coll Cardiol. 1991; 17(3):712–716. [PubMed: 1993792]
5. Svensson LG, Kim K-H, Blackstone EH, Rajeswaran J, Gillinov AM, Mihaljevic T, Griffin BP, Grimm R, Stewart WJ, Hammer DF, Lytle BW. Bicuspid aortic valve surgery with proactive ascending aorta repair. The Journal of Thoracic and Cardiovascular Surgery. 2011; 142(3):622–629. e623. [PubMed: 21292285]
6. Della Corte A, Body SC, Booher AM, Schaefers HJ, Milewski RK, Michelena HI, Evangelista A, Pibarot P, Mathieu P, Limongelli G, Shekar PS, Aranki SF, Ballotta A, Di Benedetto G, Sakalihasan N, Nappi G, Eagle KA, Bavaria JE, Frigiola A, Sundt TM. on behalf of the International Bicuspid Aortic Valve Consortium I. Surgical treatment of bicuspid aortic valve disease: Knowledge gaps and research perspectives. J Thorac Cardiovasc Surg. 2014
7. Verma S, Yanagawa B, Kalra S, Ruel M, Peterson MD, Yamashita MH, Fagan A, Currie ME, White CW, Wai Sang SL, Rosu C, Singh S, Mewhort H, Gupta N, Fedak PWM. Knowledge, attitudes, and practice patterns in surgical management of bicuspid aortopathy: A survey of 100 cardiac surgeons. The Journal of thoracic and cardiovascular surgery. 2013; 146(5):1033–1040. e1034. [PubMed: 23988289]
8. Nishimura RA, Otto CM, Bonow RO, Carabello BA, Erwin JP 3rd, Guyton RA, O'Gara PT, Ruiz CE, Skubas NJ, Sorajja P, Sundt TM 3rd, Thomas JD. 2014 AHA/ACC Guideline for the Management of Patients With Valvular Heart Disease: Executive Summary: A Report of the American College of Cardiology/American Heart Association Task Force on Practice Guidelines. J Am Coll Cardiol. 2014
9. Hiratzka LF, Bakris GL, Beckman JA, Bersin RM, Carr VF, Casey DE Jr. Eagle KA, Hermann LK, Isselbacher EM, Kazerooni EA, Kouchoukos NT, Lytle BW, Milewicz DM, Reich DL, Sen S, Shinn JA, Svensson LG, Williams DM. American College of Cardiology Foundation/American Heart Association Task Force on Practice G, American Association for Thoracic S, American College of R, American Stroke A, Society of Cardiovascular A, Society for Cardiovascular A, Interventions, Society of Interventional R, Society of Thoracic S, Society for Vascular M. 2010 ACCF/AHA/AATS/ACR/ASA/SCA/SCAI/SIR/STS/SVM Guidelines for the diagnosis and management of patients with thoracic aortic disease. A Report of the American College of Cardiology Foundation/American Heart Association Task Force on Practice Guidelines, American Association for Thoracic Surgery, American College of Radiology,American Stroke Association, Society of Cardiovascular Anesthesiologists, Society for Cardiovascular Angiography and Interventions, Society of Interventional Radiology, Society of Thoracic Surgeons,and Society for Vascular Medicine. J Am Coll Cardiol. 2010; 55(14):e27–e129. [PubMed: 20359588]
10. Fedak PW, Verma S. The molecular fingerprint of bicuspid aortopathy. J Thorac Cardiovasc Surg. 2013; 145(5):1334. [PubMed: 23597625]
11. Fedak PW. Bicuspid aortic valve syndrome: heterogeneous but predictable? Eur Heart J. 2008; 29(4):432–433. [PubMed: 18174205]

12. de Sa M, Moshkovitz Y, Butany J, David TE. Histologic abnormalities of the ascending aorta and pulmonary trunk in patients with bicuspid aortic valve disease: clinical relevance to the ross procedure. J Thorac Cardiovasc Surg. 1999; 118(4):588–594. [PubMed: 10504620]
13. Niwa K, Perloff JK, Bhuta SM, Laks H, Drinkwater DC, Child JS, Miner PD. Structural abnormalities of great arterial walls in congenital heart disease: light and electron microscopic analyses. Circulation. 2001; 103(3):393–400. [PubMed: 11157691]
14. Balistreri CR, Pisano C, Candore G, Maresi E, Codispoti M, Ruvolo G. Focus on the unique mechanisms involved in thoracic aortic aneurysm formation in bicuspid aortic valve versus tricuspid aortic valve patients: clinical implications of a pilot study. European Journal of Cardio-Thoracic Surgery. 2013; 43(6):e180–e186. [PubMed: 23248206]
15. Malek AM, Alper SL, Izumo S. Hemodynamic shear stress and its role in atherosclerosis. Journal of the American Medical Association. 1999; 282(21):2035–2042. [PubMed: 10591386]
16. Girdauskas E, Borger MA, Secknus MA, Girdauskas G, Kuntze T. Is aortopathy in bicuspid aortic valve disease a congenital defect or a result of abnormal hemodynamics? A critical reappraisal of a one-sided argument. Eur J Cardiothorac Surg. 2011; 39(6):809–814. [PubMed: 21342769]
17. Barker AJ, Markl M, Burk J, Lorenz R, Bock J, Bauer S, Schulz-Menger J, von Knobelsdorff-Brenkenhoff F. Bicuspid aortic valve is associated with altered wall shear stress in the ascending aorta. Circ Cardiovasc Imaging. 2012; 5(4):457–466. [PubMed: 22730420]
18. Barker AJ, Lanning C, Shandas R. Quantification of hemodynamic wall shear stress in patients with bicuspid aortic valve using phase-contrast MRI. Ann Biomed Eng. 2010; 38(3):788–800. [PubMed: 19953319]
19. Meierhofer C, Schneider EP, Lyko C, Hutter A, Martinoff S, Markl M, Hager A, Hess J, Stern H, Fratz S. Wall shear stress and flow patterns in the ascending aorta in patients with bicuspid aortic valves differ significantly from tricuspid aortic valves: a prospective study. European Heart Journal - Cardiovascular Imaging. 2012; 14(8):797–804. [PubMed: 23230276]
20. Bissell MM, Hess AT, Biasiolli L, Glaze SJ, Loudon M, Pitcher A, Davis A, Prendergast B, Markl M, Barker AJ, Neubauer S, Myerson SG. Aortic dilation in bicuspid aortic valve disease: flow pattern is a major contributor and differs with valve fusion type. Circ Cardiovasc Imaging. 2013; 6(4):499–507. [PubMed: 23771987]
21. Stalder A, Russe M, Frydrychowicz A, Bock J, Hennig J, Markl M. Quantitative 2D and 3D phase contrast MRI: Optimized analysis of blood flow and vessel wall parameters. Magn Reson Med. 2008; 60(5):1218–1231. [PubMed: 18956416]
22. Bieging ET, Frydrychowicz A, Wentland A, Landgraf BR, Johnson KM, Wieben O, Francois CJ. In vivo three-dimensional MR wall shear stress estimation in ascending aortic dilatation. J Magn Reson Imaging. 2011; 33(3):589–597. [PubMed: 21563242]
23. Potters WV, van Ooij P, Marquering HA, Van Bavel ET, Nederveen AJ. Volumetric arterial wall shear stress calculation based on cine phase contrast MRI. JMRI. 2013
24. van Ooij P, Potters WV, Nederveen AJ, Allen BD, Collins J, Carr J, Malaisrie SC, Markl M, Barker AJ. A Methodology to Detect Abnormal Relative Wall Shear Stress on the Full Surface of the Thoracic Aorta Using 4D Flow MRI. Magnetic Resonance in Medecine. 2014
25. Markl M, Harloff A, Bley TA, Zaitsev M, Jung B, Weigang E, Langer M, Hennig J, Frydrychowicz A. Time-resolved 3D MR velocity mapping at 3T: improved navigator-gated assessment of vascular anatomy and blood flow. J Magn Reson Imaging. 2007; 25(4):824–831. [PubMed: 17345635]
26. Entezari P, Schnell S, Mahadevia R, Malaisrie C, McCarthy P, Mendelson M, Collins J, Carr JC, Markl M, Barker AJ. From unicuspid to quadricuspid: Influence of aortic valve morphology on aortic three-dimensional hemodynamics. J Magn Reson Imaging. 2013
27. Fazel SS, Mallidi HR, Lee RS, Sheehan MP, Liang D, Fleischman D, Herfkens R, Mitchell RS, Miller DC. The aortopathy of bicuspid aortic valve disease has distinctive patterns and usually involves the transverse aortic arch. J Thorac Cardiovasc Surg. 2008; 135(4):901–907. 907, e901–e902. [PubMed: 18374778]
28. Kang JW, Song HG, Yang DH, Baek S, Kim DH, Song JM, Kang DH, Lim TH, Song JK. Association between bicuspid aortic valve phenotype and patterns of valvular dysfunction and

bicuspid aortopathy: comprehensive evaluation using MDCT and echocardiography. JACC Cardiovasc Imaging. 2013; 6(2):150–161. [PubMed: 23489528]

29. Entezari P, kino A, Honarmand AR, Galizia MS, Yang Y, Collins J, Yaghmai V, Carr JC. Analysis of the thoracic aorta using a semi-automated post processing tool. European Journal of Radiology. 2013; 82(9):1558–1564. [PubMed: 23680155]
30. Bonow RO, Carabello BA, Chatterjee K, de Leon AC Jr. Faxon DP, Freed MD, Gaasch WH, Lytle BW, Nishimura RA, O'Gara PT, O'Rourke RA, Otto CM, Shah PM, Shanewise JS. American College of Cardiology/American Heart Association Task Force on Practice G. 2008 focused update incorporated into the ACC/AHA 2006 guidelines for the management of patients with valvular heart disease: a report of the American College of Cardiology/American Heart Association Task Force on Practice Guidelines (Writing Committee to revise the 1998 guidelines for the management of patients with valvular heart disease). Endorsed by the Society of Cardiovascular Anesthesiologists, Society for Cardiovascular Angiography and Interventions, and Society of Thoracic Surgeons. J Am Coll Cardiol. 2008; 52(13):e1–142. [PubMed: 18848134]
31. Bock J, Kreher W, Hennig J, Markl M. Optimized pre-processing of time-resolved 2D and 3D Phase Contrast MRI data. Proc Intl Soc Mag Reson Med. 2007; 15:3138.
32. Unser M. Splines: a perfect fit for signal and image processing. Signal Processing Magazine, IEEE. 1999; 16(6):22–38.
33. Jenkinson M, Smith S. A global optimisation method for robust affine registration of brain images. Med Image Anal. 2001; 5(2):143–156. [PubMed: 11516708]
34. Verma S, Siu SC. Aortic dilatation in patients with bicuspid aortic valve. N Engl J Med. 2014; 370(20):1920–1929. [PubMed: 24827036]
35. Chandran KB, Vigmostad SC. Patient-specific bicuspid valve dynamics: overview of methods and challenges. J Biomech. 2013; 46(2):208–216. [PubMed: 23182904]
36. Conti CA, Della Corte A, Votta E, Del Viscovo L, Bancone C, De Santo LS, Redaelli A. Biomechanical implications of the congenital bicuspid aortic valve: a finite element study of aortic root function from in vivo data. J Thorac Cardiovasc Surg. 2010; 140(4):890–896. 896, e891–e892. [PubMed: 20363481]
37. Viscardi F, Vergara C, Antiga L, Merelli S, Veneziani A, Puppini G, Faggian G, Mazzucco A, Luciani GB. Comparative Finite Element Model Analysis of Ascending Aortic Flow in Bicuspid and Tricuspid Aortic Valve. Artificial Organs. 2010; 34(12):1114–1120. [PubMed: 20618222]
38. Keshavarz-Motamed Z, Garcia J, Kadem L. Fluid dynamics of coarctation of the aorta and effect of bicuspid aortic valve. PLoS One. 2013; 8(8):e72394. [PubMed: 24015239]
39. Faggiano E, Antiga L, Puppini G, Quarteroni A, Luciani GB, Vergara C. Helical flows and asymmetry of blood jet in dilated ascending aorta with normally functioning bicuspid valve. Biomech Model Mechanobiol. 2013; 12(4):801–813. [PubMed: 23053594]
40. Morbiducci U, Ponzini R, Gallo D, Bignardi C, Rizzo G. Inflow boundary conditions for image-based computational hemodynamics: impact of idealized versus measured velocity profiles in the human aorta. J Biomech. 2013; 46(1):102–109. [PubMed: 23159094]
41. Brown AG, Shi Y, Marzo A, Staicu C, Valverde I, Beerbaum P, Lawford PV, Hose DR. Accuracy vs. computational time: Translating aortic simulations to the clinic. Journal of Biomechanics. 2012; 45(3):516–523. [PubMed: 22189248]
42. Atkins S, Cao K, Rajamannan N, Sucosky P. Bicuspid aortic valve hemodynamics induces abnormal medial remodeling in the convexity of porcine ascending aortas. Biomech Model Mechanobiol. 2014:1–17.
43. Tzemos N, Lyseggen E, Silversides C, Jamorski M, Tong JH, Harvey P, Floras J, Siu S. Endothelial Function, Carotid-Femoral Stiffness, and Plasma Matrix Metalloproteinase-2 in Men With Bicuspid Aortic Valve and Dilated Aorta. Journal of the American College of Cardiology. 2010; 55(7):660–668. [PubMed: 20170792]
44. Mohamed SA, Noack F, Schoellermann K, Karluss A, Radtke A, Schult-Badusche D, Radke PW, Wenzel BE, Sievers HH. Elevation of matrix metalloproteinases in different areas of ascending aortic aneurysms in patients with bicuspid and tricuspid aortic valves. TheScientificWorldJournal. 2012

45. Aicher D, Urbich C, Zeiher A, Dimmeler S, Schäfers H-J. Endothelial Nitric Oxide Synthase in Bicuspid Aortic Valve Disease. The Annals of Thoracic Surgery. 2007; 83(4):1290–1294. [PubMed: 17383329]

46. Mohamed SA, Radtke A, Saraei R, Bullerdiek J, Sorani H, Nimzyk R, Karluss A, Sievers HH, Belge G. Locally different endothelial nitric oxide synthase protein levels in ascending aortic aneurysms of bicuspid and tricuspid aortic valve. Cardiology research and practice. 2012

47. Hope MD, Hope TA, Meadows AK, Ordovas KG, Urbania TH, Alley MT, Higgins CB. Bicuspid aortic valve: four-dimensional MR evaluation of ascending aortic systolic flow patterns. Radiology. 2010; 255(1):53. [PubMed: 20308444]

48. Hope MD, Sigovan M, Wrenn SJ, Saloner D, Dyverfeldt P. MRI hemodynamic markers of progressive bicuspid aortic valve-related aortic disease. Journal of Magnetic Resonance Imaging. 2013

49. Burk J, Blanke P, Stankovic Z, Barker A, Russe M, Geiger J, Frydrychowicz A, Langer M, Markl M. Evaluation of 3D blood flow patterns and wall shear stress in the normal and dilated thoracic aorta using flow-sensitive 4D CMR. J Cardiovasc Magn Reson. 2012; 14:84. [PubMed: 23237187]

50. Girdauskas E, Rouman M, Disha K, Scholle T, Fey B, Theis B, Petersen I, Borger MA, Kuntze T. Correlation between systolic transvalvular flow and proximal aortic wall changes in bicuspid aortic valve stenosis. Eur J Cardiothorac Surg. 2014 [E-pub ahead of print].

51. Mahadevia R, Barker AJ, Schnell S, Entezari P, Kansal P, Fedak PW, Malaisrie SC, McCarthy P, Collins J, Carr J, Markl M. Bicuspid aortic cusp fusion morphology alters aortic three-dimensional outflow patterns, wall shear stress, and expression of aortopathy. Circulation. 2014; 129(6):673–682. [PubMed: 24345403]

52. Strecker C, Harloff A, Wallis W, Markl M. Flow-sensitive 4D MRI of the thoracic aorta: Comparison of image quality, quantitative flow, and wall parameters at 1.5 T and 3 T. Journal of Magnetic Resonance Imaging. 2012; 36(5):1097–1103. [PubMed: 22745007]

53. Potters W, Marquering H, VanBavel E, Nederveen A. Measuring Wall Shear Stress Using Velocity-Encoded MRI. Curr Cardiovasc Imaging Rep. 2014; 7(4):1–12.

54. Cibis M, Potters WV, Gijsen FJ, Marquering H, vanBavel E, van der Steen AF, Nederveen AJ, Wentzel JJ. Wall shear stress calculations based on 3D cine phase contrast MRI and computational fluid dynamics: a comparison study in healthy carotid arteries. NMR Biomed. 2014; 27(7):826–834. [PubMed: 24817676]

55. van Ooij P, Potters WV, Guedon A, Schneiders JJ, Marquering HA, Majoie CB, Vanbavel E, Nederveen AJ. Wall shear stress estimated with phase contrast MRI in an in vitro and in vivo intracranial aneurysm. J Magn Reson Imaging. 2013; 38(4):876–884. [PubMed: 23417769]

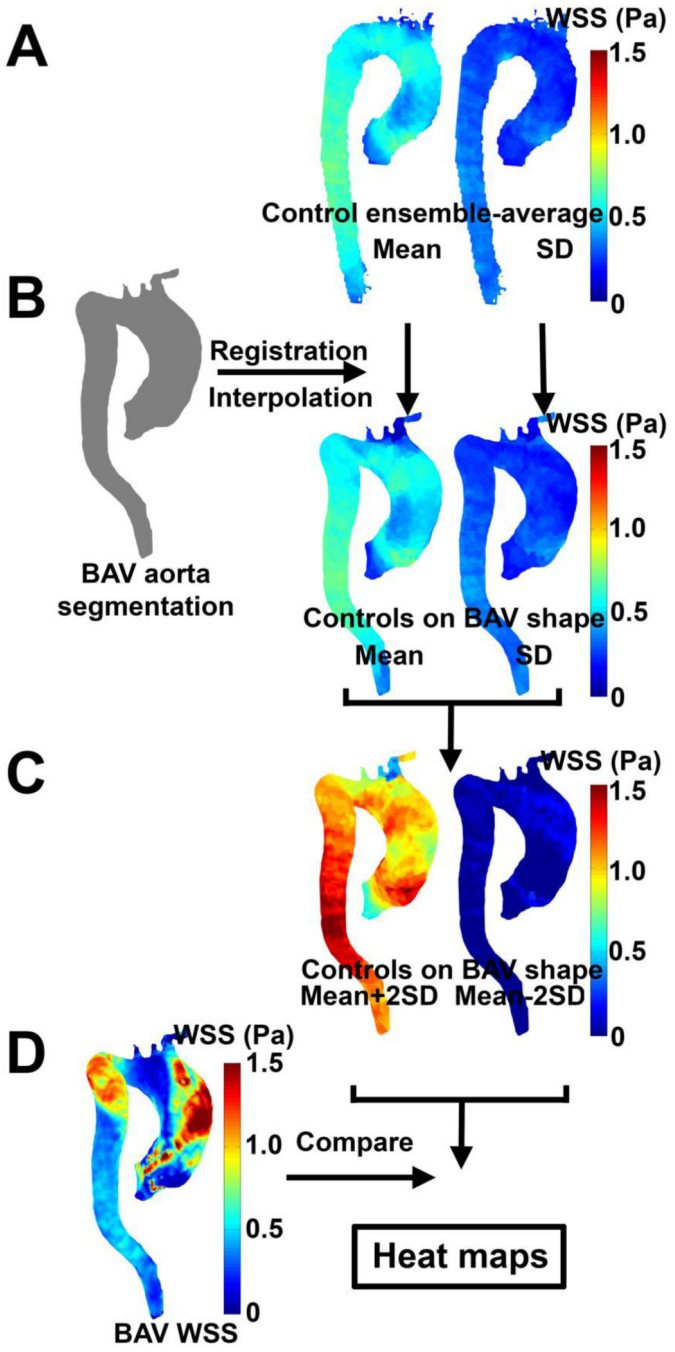

Figure 1.

Generation of WSS heat maps. (A) The control population-averaged mean and SD WSS maps were registered and interpolated to the aorta segmentation of the BAV patient (B). (C) The mean ± 1.96 times SD maps are created and compared with the peak systolic WSS of the BAV patients resulting in the heat maps (D).

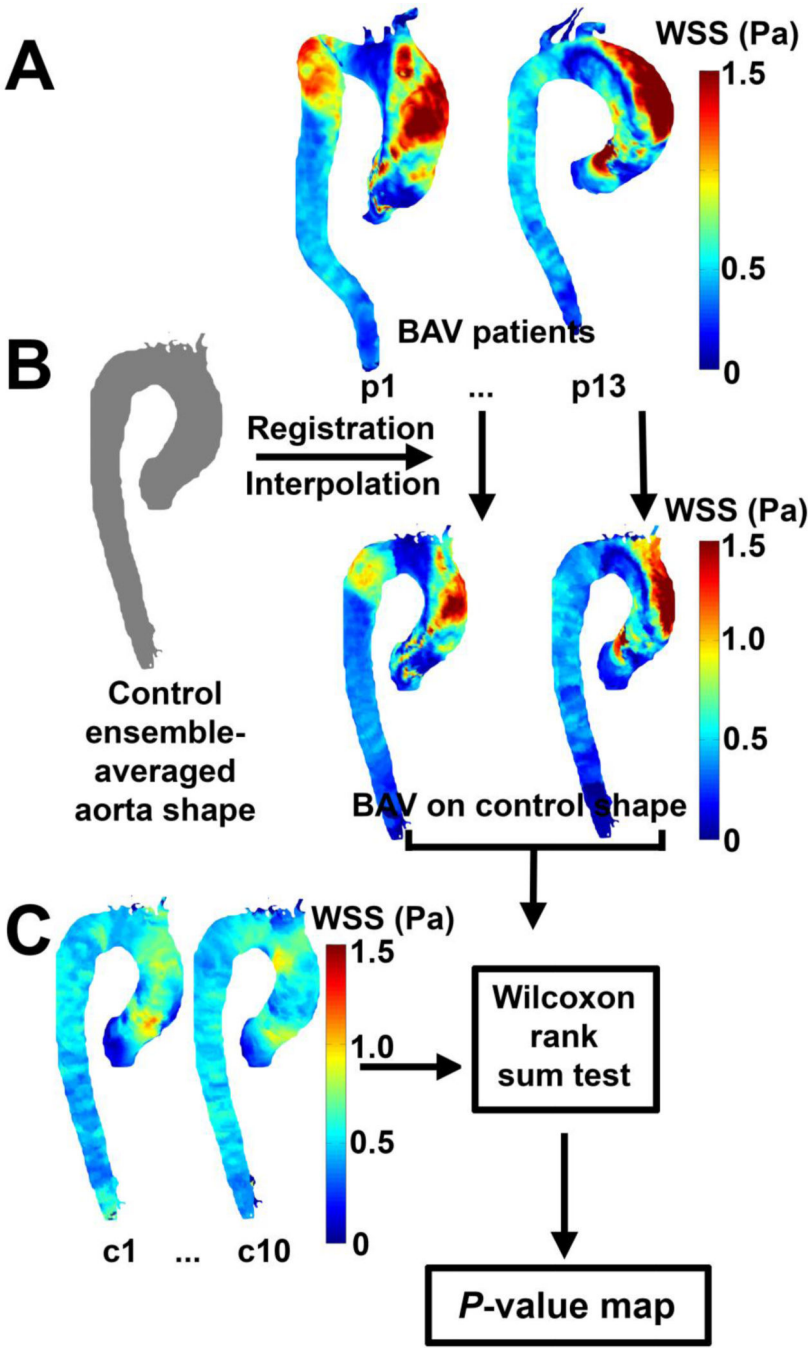

Figure 2.

Generation of WSS P-value maps. (A) The individual systolic WSS maps were registered and interpolated to the control population averaged aorta geometry (B). (C) A Wilcoxon rank sum test was performed between the individual controls and the BAV patients to create the P-value maps.

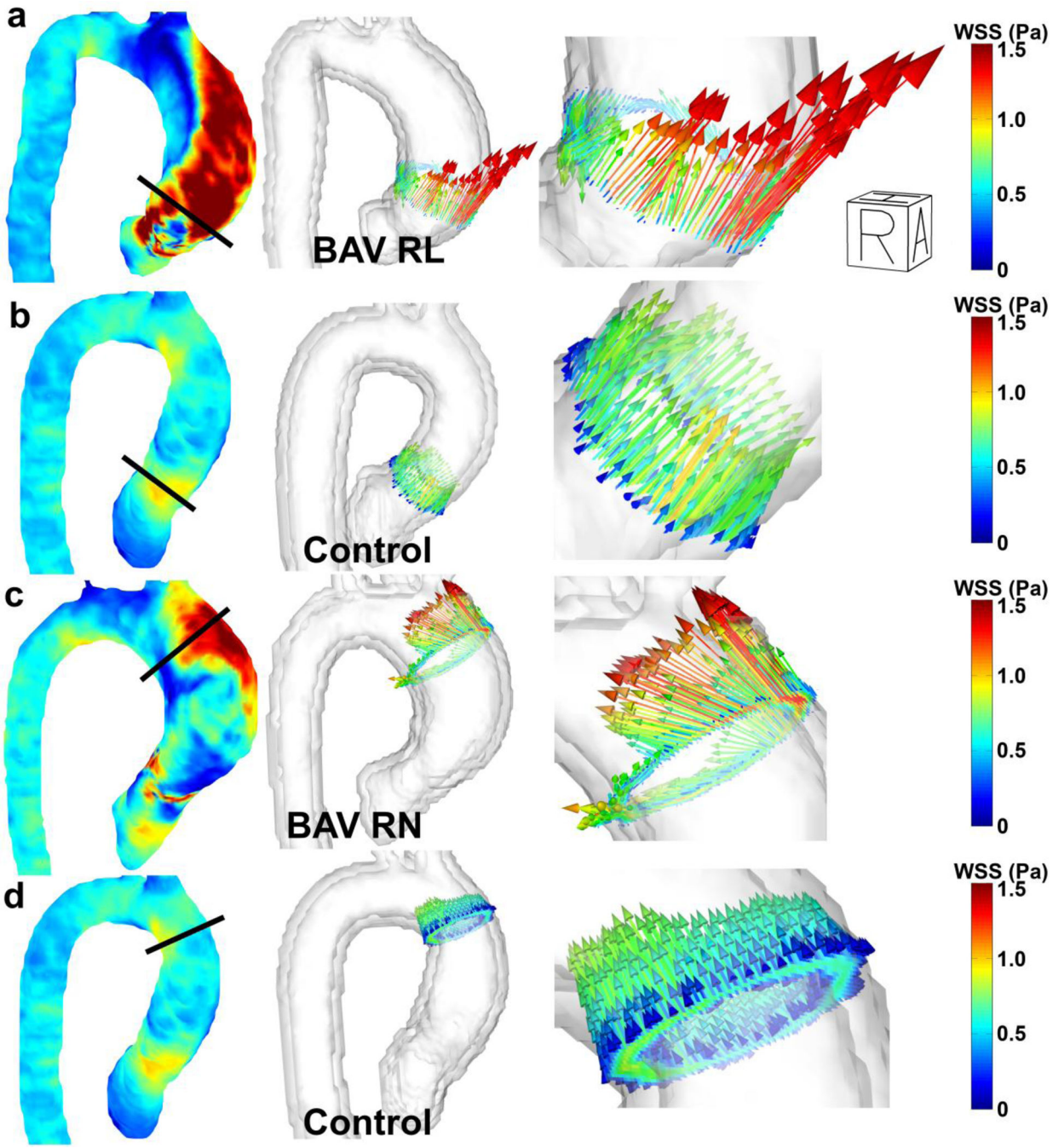

Figure 3.

Peak systolic volumetric WSS velocity vectors (column 1) and WSS vectors in slices manually placed orthogonal in the ascending aorta (column 2 and 3) for (a) a BAV patient with RL fusion, (b) a control with the slice positioned similar to (a), (c) a BAV patient with RN fusion and (d) the same control subject with the slice positioned similar to (d).

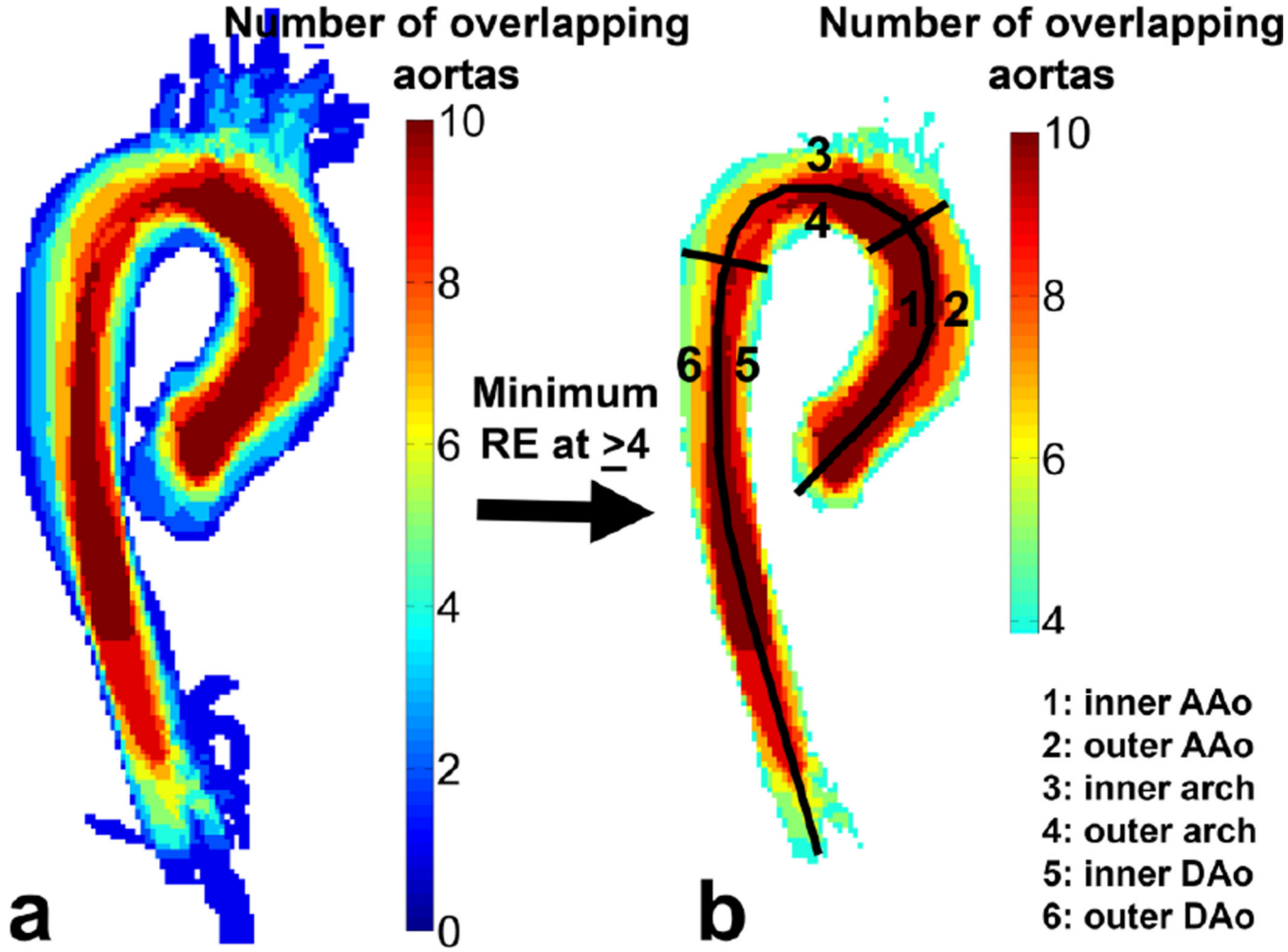

Figure 4.

(a) A map representing the overlap of all 10 control aortas. (b) The idealized geometry is the overlap map where the overlap is maximized over the subjects: in this case where more than 4 aortas are overlapping. The six regions where the difference in velocity before and after interpolation and the percentage of surface area with abnormal WSS was calculated is shown in (b) as well: 1) Inner curvature AAo, 2) Outer curvature AAo, 3) Inner curvature Arch, 4) Outer curvature Arch, 5) Inner curvature DAo and 6) Outer curvature DAo.

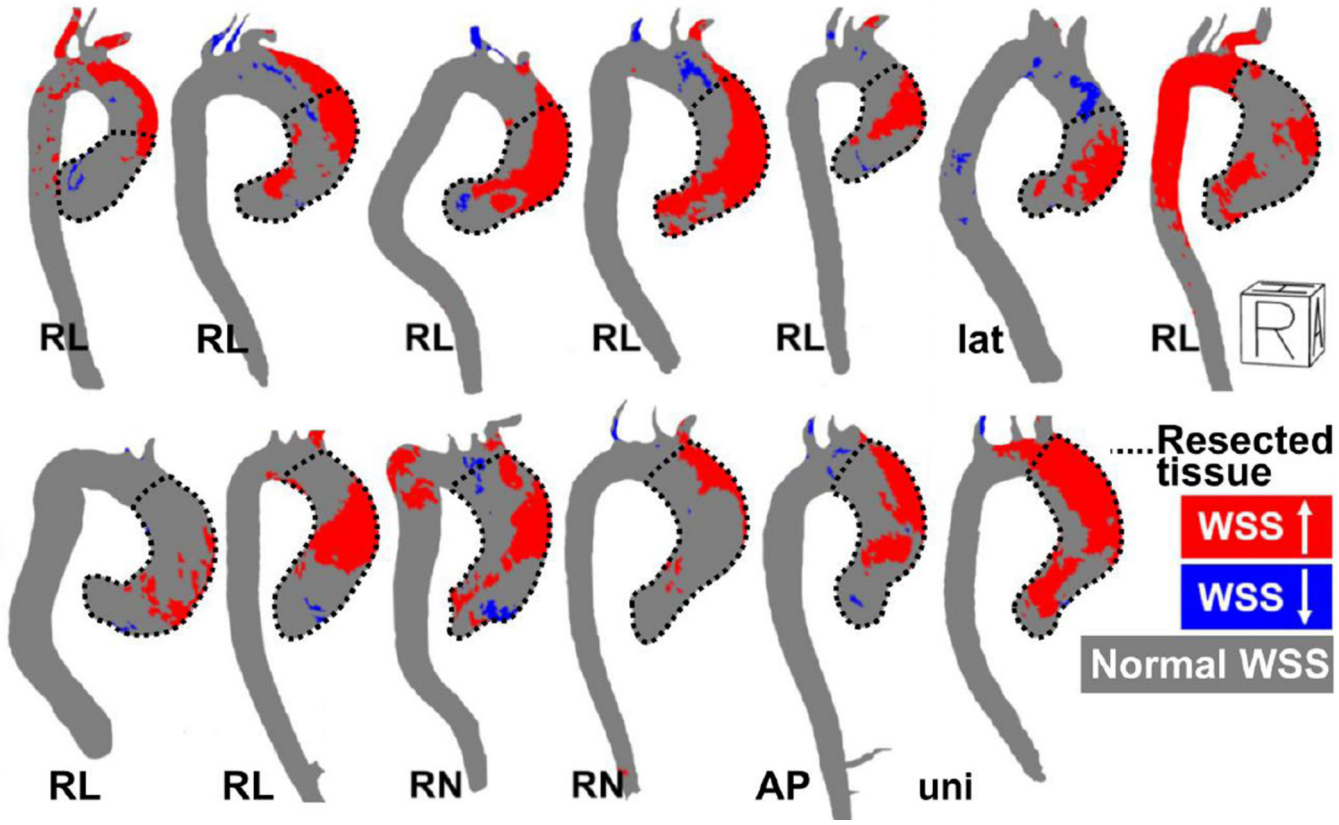

Figure 5.

Right-anterior oblique views of the WSS heat maps illustrating abnormally elevated WSS (red) and depressed WSS (blue). RL indicates BAV patients with fusion of the right and left coronary cusps, RN indicates BAV patients with fusion of the right and non-coronary cusp. Lat indicates a valve without raphe that opens in lateral direction and uni indicates a functionally unicuspid valve with two raphes. R = Right, A = Anterior, H = Head.

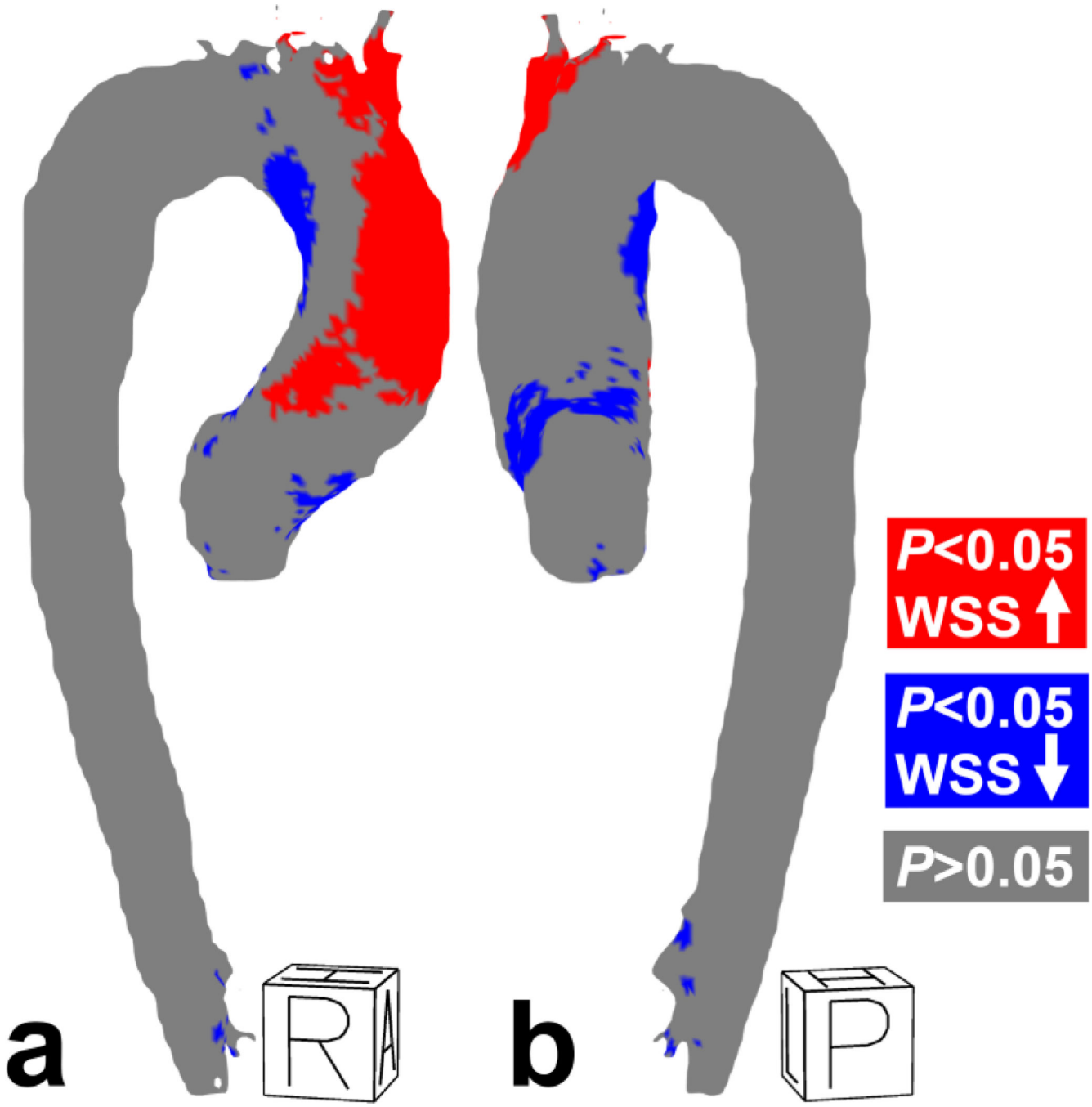

Figure 6.

(a) Right-anterior and (b) posterior-right views of the P-value map for WSS. R = Right, A = Anterior, H = Head, P = Posterior, R = Right

Table 1

Aortic dimensions, valve morphology, aortopathy phenotype, aortic insufficiency and aortic stenosis of the BAV patients and the controls. Differences across cohorts were evaluated using a Wilcoxon rank sum test.

	Patients with BAV		Normal Controls	*P*-value
SOV diameter (cm)	4.5±0.6		3.0±0.5	<0.001
MAA diameter (cm)	4.7±0.7		2.9±0.5	<0.001
Heart rate (bpm)	74±17		74±15	0.80
Cardiac output (L/min)	8±3		6±2	0.10
Body surface area (m^2)	2.0±0.2		1.9±0.2	0.28
Valve morphology	AP	1	TAV	
	Lat	1		
	RL	8		
	RN	2		
	uni	1		
Aortopathy phenotype	ATP 0	0	N/A	
	ATP 1	1		
	ATP 2	6		
	ATP 3	6		
Aortic insufficiency	Mild	4	N/A	
	Moderate	5		
	Severe	4		
Aortic stenosis	None	2	N/A	
	Mild	6		
	Moderate	0		
	Severe	5		

SOV = Sinus of Valsalva, MAA = Mid-ascending Aorta, AP = Anterior-Posterior, Lat = Lateral, RL = Right-Left, RN = Right-Non-coronary, NL = Non-coronary-Left, ATP=Aortopathy type

Table 2

Percentage of the surface area in BAV subjects (mean ± standard deviation) which exceed normal WSS values (in the six regions of interest schematically shown in figure 4). Subjects are categorized according to valve phenotype.

	Surface percentage of increased WSS (%)				
	AP (n=1)	**lat (n=1)**	**RL (n=8)**	**RN (n=2)**	**uni (n=1)**
1. Inner AAo	9 ± 0	8 ± 0	14 ± 8	17 ± 2	29 ± 0
2. Outer AAo	29 ± 0	22 ± 0	35 ± 18	34 ± 6	49 ± 0
3. Inner arch	0 ± 0	0 ± 0	17 ± 29	2 ± 3	9 ± 0
4. Outer arch	10 ± 0	0 ± 0	20 ± 27	18 ± 4	30 ± 0
5. Inner DAo	0 ± 0	0 ± 0	6 ± 14	0 ± 0	0 ± 0
6. Outer DAo	0 ± 0	0 ± 0	4 ± 11	0 ± 0	0 ± 0

Table 3

The surface percentages of the six regions of interest (see figure 4) for the WSS P-value map.

	Surface percentage of	
	Increased WSS (%)	**Decreased WSS (%)**
1.Inner AAo	7	14
2. Outer AAo	33	10
3. Inner Arch	0	8
4. Outer Arch	25	0
5. Inner DAo	0	1
6. Outer DAo	0	0